arXiv:0711.3504v1 [nucl-th] 22 Nov 2007

International Journal of Modern Physics E
© World Scientific Publishing Company

NON-UNIFORM STRUCTURE OF MATTER AND THE EQUATION OF STATE

TOSHIKI MARUYAMA
Advanced Science Research Center, Japan Atomic Energy Agency,
Shirakata Shirane 2-4, Tokai, Ibaraki 319-1195, Japan
maruyama.toshiki@jaea.go.jp

SATOSHI CHIBA
Advanced Science Research Center, Japan Atomic Energy Agency,
Shirakata Shirane 2-4, Tokai, Ibaraki 319-1195, Japan

TOSHITAKA TATSUMI
Department of Physics, Kyoto University, Kyoto 606-8502, Japan

Received (received date)
Revised (revised date)

We investigate the non-uniform structures and the equation of state (EOS) of nuclear matter in the context of the first-order phase transitions (FOPT) such as liquid-gas phase transition, kaon condensation, and hadron-quark phase transition. During FOPT the mixed phases appear, where matter exhibits non-uniform structures called "Pasta" structures due to the balance of the Coulomb repulsion and the surface tension between two phases. We treat these effects self-consistently, properly taking into account of the Poisson equation and the Gibbs conditions. Consequently, they make the EOS of the mixed phase closer to that of Maxwell construction due to the Debye screening. This is a general feature of the mixed phase consisting of many species of charged particles.

1. Introduction

Matter in stellar objects has a variety of densities and chemical components due to the presence of gravity. At the surface of neutron stars, there exists a region where the density is lower than the normal nuclear density $\rho_0 \simeq 0.16\text{fm}^{-3}$ over a couple of hundreds meters. The pressure of such matter is retained by degenerate electrons, while baryons are clusterized and have little contribution to the pressure. Due to the gravity the pressure and the density increase in the inner region (in fact, the density at the center amounts to several times ρ_0). Charge neutral matter consists of neutrons and the equal number of protons and electrons under chemical equilibrium. Since the kinetic energy of degenerate electrons is much higher than that of baryons, the electron fraction (or the proton one) decreases with increase of density and thus neutrons become the main component and drip out of the clusters. In this way baryons as well as electrons come to contribute to the pressure. At

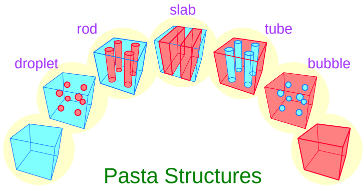

Fig. 1. Schematic picture of pasta structures. Phase transition from blue phase (left-bottom) to red phase (right-bottom) is considered.

a certain density, other components such as hyperons and mesons may emerge. For example, negative kaon condensation, expected to be of a first-order phase transition (FOPT), remarkably softens the equation of state of matter. At even higher density, hadron-quark deconfinement transition may occur and quarks in hadrons are liberated. This phase transition is also considered to be of first-order.

A FOPT brings about a thermodynamic instability of uniform matter to have phase separation. In other words, matter should have the nonuniform mixed phase (MP) around the critical density. Since nuclear matter consists of two chemically independent components, i.e. baryons and electrons, the equalities of both baryon and electron chemical potentials between two phases are required by the Gibbs conditions in the MP. Therefore the EOS of the MP cannot be obtained simply by the Maxwell construction, which is relevant only for single component. Those components are electrically charged and non-uniformly distributed, so that the local charge neutrality is no more held in the MP. This point is important to the geometrical structure of the MP. To minimize the surface energy plus the Coulomb energy, matter is expected to form a structured mixed phase, i.e. a lattice of lumps of a phase with a geometrical symmetry embedded in the other phase.

At very low densities, nuclei in matter are expected to form the Coulomb lattice embedded in the electron sea, that minimizes the Coulomb interaction energy. With increase of density, "nuclear pasta" structures (see Fig. 1) emerge as a structured mixed phase[1] in the liquid-gas phase transition, where stable nuclear shape may change from droplet to rod, slab, tube, and to bubble. Pasta nuclei are eventually dissolved into uniform matter at a certain nucleon density below the saturation density ρ_0. The name "pasta" comes from rod and slab structures figuratively spoken as "spaghetti" and "lasagna". Such low-density nuclear matter exists in the collapsing stage of supernovae and in the crust of neutron stars. Supernova matter is relevant to liquid-gas transition of non-beta-equilibrium nuclear matter with a fixed proton fraction and the low-density neutron star matter is relevant to neutron-drip transition of beta-equilibrium nuclear matter. The structured mixed phase is also expected in the phase transitions at higher density, like kaon condensation and hadron-quark phase transition. In these cases, the charge screening effect may be pronounced because the local charge density can be high.

Our purpose here is to investigate low-density nuclear pasta structure, kaonic pasta structure, and hadron-quark pasta structure self-consistently within the mean-field approximation. In particular, we figure out how the Coulomb screening and the surface tension affect the property of the MP.

2. Low Density Nuclear Matter

First we investigate the property of nuclear matter at low density. Exploiting the idea of the density functional theory within the relativistic mean field (RMF) model, we can formulate equations of motion to study non-uniform nuclear matter numerically, cf. Refs. 2, 3. The RMF model with fields of mesons and baryons introduced in a Lorentz-invariant way is not only relatively simple for numerical calculations, but also sufficiently realistic to reproduce bulk properties of finite nuclei as well as the saturation properties of nuclear matter.[4,5] In our framework, the Coulomb interaction is properly included in the equations of motion for nucleons and electrons and for meson mean fields, and we solve the Poisson equation for the Coulomb potential V self-consistently with those equations. Thus the baryon and electron density profiles, as well as the meson mean fields, are determined in a fully consistent way with the Coulomb interaction.

2.1. *Relativistic mean field model*

2.1.1. *Thermodynamic potential and the equations of motion*

We start with the thermodynamic potential for the system of neutrons, protons, electrons and mesons with temperature $T = 0$,

$$\Omega = \Omega_N + \Omega_M + \Omega_e. \tag{1}$$

The first term is the contribution of nucleons with the local-density approximation,

$$\Omega_N = \sum_{a=p,n} \int d^3r \left[\int_0^{k_{\mathrm{F},a}} \frac{d^3k}{4\pi^3} \sqrt{{m_N^*}^2 + k^2} - \rho_a \nu_a \right], \tag{2}$$

$$\nu_n(\mathbf{r}) = \mu_n - g_{\omega N}\omega_0(\mathbf{r}) + g_{\rho N} R_0(\mathbf{r}), \tag{3}$$

$$\nu_p(\mathbf{r}) = \mu_p + V(\mathbf{r}) - g_{\omega N}\omega_0(\mathbf{r}) - g_{\rho N} R_0(\mathbf{r}), \tag{4}$$

with the local Fermi momenta $k_{\mathrm{F},a}(\mathbf{r})$ $(a = n, p)$, the effective nucleon mass $m_N^*(\mathbf{r}) = m_N - g_{\sigma N}\sigma(\mathbf{r})$, the chemical potentials μ_a $(a = n, p)$, and coupling constants $g_{\sigma N}$, $g_{\omega N}$ and $g_{\rho N}$.

The second term in (1) includes the scalar (σ) and vector (ω_0, R_0) mean fields,

$$\Omega_M = \int d^3r \left[\frac{(\nabla\sigma)^2 + m_\sigma^2\sigma^2}{2} + U(\sigma) - \frac{(\nabla\omega_0)^2 + m_\omega^2\omega_0^2}{2} - \frac{(\nabla R_0)^2 + m_\rho^2 R_0^2}{2} \right], \tag{5}$$

where m_σ, m_ω and m_ρ are the field masses, and $U(\sigma) = \frac{1}{3} b m_N (g_{\sigma N}\sigma)^3 + \frac{1}{4} c (g_{\sigma N}\sigma)^4$ is the nonlinear potential for the scalar field.

The third term in (1) contains the contribution of the Coulomb field (described by the potential $V(\mathbf{r})$) and the contribution of relativistic electrons,

$$\Omega_e = \int d^3r \left[-\frac{1}{8\pi e^2} (\nabla V)^2 - \frac{(\mu_e - V)^4}{12\pi^2} \right], \tag{6}$$

where μ_e is the electron chemical potential.

Table 1. Parameter set used in RMF calculation in Secs. 2 and 3. The kaon optical potential U_K is defined by $U_K = g_{\sigma K}\sigma + g_{\omega K}\omega_0$.

$g_{\sigma N}$	$g_{\omega N}$	$g_{\rho N}$	b	c	m_σ	m_ω
6.3935	8.7207	4.2696	0.008659	0.002421	400 MeV	783 MeV

m_ρ	$f_K(\approx f_\pi)$	m_K	$g_{\omega K}$	$g_{\rho K}$	$U_K(\rho_0)$
769 MeV	93 MeV	494 MeV	$g_{\omega N}/3$	$g_{\rho N}$	-130 MeV

Equations of motion for the fields are obtained from the variational principle,

$$\nabla^2\sigma(\mathbf{r}) = m_\sigma^2\sigma(\mathbf{r}) + \frac{dU}{d\sigma} - g_{\sigma N}(\rho_n^s(\mathbf{r}) + \rho_p^s(\mathbf{r})), \tag{7}$$

$$\nabla^2\omega_0(\mathbf{r}) = m_\omega^2\omega_0(\mathbf{r}) - g_{\omega N}(\rho_p(\mathbf{r}) + \rho_n(\mathbf{r})), \tag{8}$$

$$\nabla^2 R_0(\mathbf{r}) = m_\rho^2 R_0(\mathbf{r}) - g_{\rho N}(\rho_p(\mathbf{r}) - \rho_n(\mathbf{r})), \tag{9}$$

$$\nabla^2 V(\mathbf{r}) = 4\pi e^2\rho_{\rm ch}(\mathbf{r}), \tag{10}$$

$$\mu_e = \left(3\pi^2\rho_e(\mathbf{r})\right)^{1/3} + V(\mathbf{r}), \tag{11}$$

$$\mu_n \;=\; \mu_B = \sqrt{k_{{\rm F},n}(\mathbf{r})^2 + m_N^*(\mathbf{r})^2} + g_{\omega N}\omega_0(\mathbf{r}) - g_{\rho N}R_0(\mathbf{r}), \tag{12}$$

$$\mu_p \;=\; \mu_B - \mu_e = \sqrt{k_{{\rm F},p}(\mathbf{r})^2 + m_N^*(\mathbf{r})^2} + g_{\omega N}\omega_0(\mathbf{r}) + g_{\rho N}R_0(\mathbf{r}) - V(\mathbf{r}). \tag{13}$$

with the proton and neutron scalar densities and the charge density

$$\rho_a^s(\mathbf{r}) = \int_0^{k_{{\rm F},a}(\mathbf{r})} \frac{d^3k}{4\pi^3}\frac{m_N^*(\mathbf{r})}{\sqrt{m_N^*(\mathbf{r})^2 + k^2}}, \quad (a = p, n), \tag{14}$$

$$\rho_{\rm ch}(\mathbf{r}) = \rho_p(\mathbf{r}) - \rho_e(\mathbf{r}). \tag{15}$$

To solve the above coupled equations numerically, the whole space is divided into equivalent Wigner-Seitz cells with a radius $R_{\rm W}$. The geometrical shape of the cell changes as follows: sphere in three-dimensional (3D) calculation, cylinder in 2D and slab in 1D, respectively. Each cell is globally charge-neutral and all physical quantities in the cell are smoothly connected to those of the next cell with zero gradients at the boundary. Every point inside the cell is represented by the grid points (number of grid points $N_{\rm grid} \approx 100$) and differential equations for fields are solved by the relaxation method for a given baryon-number density under constraints of the global charge neutrality. Details of the numerical procedure are explained in Refs. 4, 5.

Parameters of the RMF model are chosen to reproduce saturation properties of symmetric nuclear matter: the minimum energy per nucleon -16.3 MeV at $\rho = \rho_0 \equiv 0.153$ fm^{-3}, the incompressibility $K(\rho_0) = 240$ MeV, the effective nucleon mass $m_N^*(\rho_0) = 0.78 m_N$; $m_N = 938$ MeV, and the isospin-asymmetry coefficient $a_{\rm sym} = 32.5$ MeV. Coupling constants and meson masses used in our calculation are listed in Table 1.

For the study of non-uniform nuclear matter, the ability to reproduce the bulk properties of finite nuclei should be essential. We have checked how it works to describe finite nuclei and we have checked that the bulk properties of finite nuclei (density, binding energy, and proton to baryon number ratio) are satisfactorily reproduced for our present purpose.[4,5]

2.1.2. *Control of surface tension*

Note that in our framework we must use a sigma mass $m_\sigma = 400$ MeV,[6] a slightly smaller value than that one usually uses, to get an appropriate fit. If we used a popular value $m_\sigma \approx 500$ MeV, finite nuclei would be over-bound by about 3 MeV/A. The actual value of the sigma mass (as well as the omega and rho masses) has little relevance for the case of infinite nucleon matter, since it enters the thermodynamic potential only in the combination $\widetilde{C}_\sigma = g_{\sigma N}/m_\sigma$. However meson masses are important characteristics of finite nuclei and of other non-uniform nucleon systems, like those in pasta. The effective meson mass characterizes the typical scale for the spatial change of the meson field and consequently it affects the value of the effective surface tension.

If we artificially multiply meson masses m_σ, m_ω and m_ρ by a factor c_M, e.g. $c_M = 1$ (realistic case), 2.5 and 5.0, the surface tension changes. By the use of heavy meson masses, the binding energy of finite nuclei (for finite A) approaches to that of nuclear matter. This shows that the surface tension is reduced with increase of the meson masses, cf. Ref. 7. Notice that this statement is correct only if we fix the ratio $g_{\phi N}^2/m_\phi^2$. Using the above modified meson masses, we explore the effects of the surface tension later.

2.2. ***Nucleon matter with fixed proton fraction***

First, we concentrate on the behavior of nucleon matter at fixed values of the proton fraction Y_p. Particularly, we explore $Y_p = 0.1$ and 0.5. The case $Y_p = 0.5$ should be relevant for supernova matter and for newly born neutron stars. Figure 2 shows some typical density profiles inside the Wigner-Seitz cells. The geometrical dimension of the cell is denoted as "3D" (three-dimensional sphere), etc. The horizontal axis in each panel denotes the radial distance from the center of the cell. The cell boundary is indicated by the hatch. From the top to the bottom the configuration corresponds to droplet (3D), rod (2D), slab (1D), tube (2D), and bubble (3D). The nuclear "pasta" structures are clearly manifested. For the lowest Y_p case ($Y_p = 0.1$), the neutron density is finite at any point: the space is filled by dripped neutrons. The value of Y_p above which neutrons drip is around 0.26 in our 3D calculation, for example. For a higher Y_p, the neutron density drops to zero outside the nucleus. The proton number density always drops to zero outside the nucleus. We can see that the charge screening effects are pronounced. Due to the spatial rearrangement of electrons the electron density profile becomes no more uniform. This non-uniformity of the electron distribution is more pronounced for a higher Y_p and a higher density.

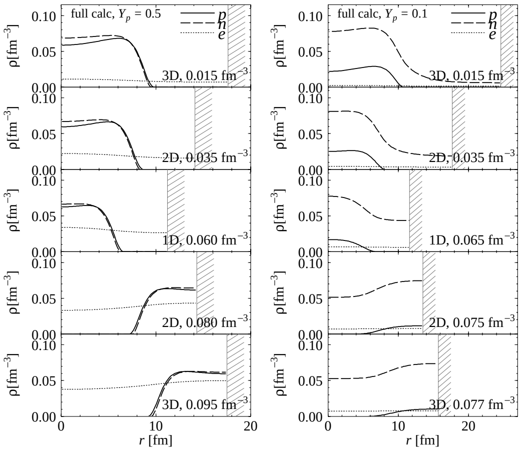

Fig. 2. Examples of the density profiles in the cell for symmetric nuclear matter with Y_p=0.5 (left) and for asymmetric matter with $Y_p = 0.1$ (right).

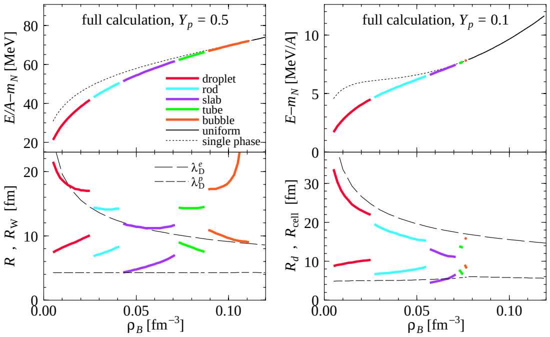

Fig. 3. Binding energy per nucleon (upper) and the cell and lump sizes (lower) for symmetric nuclear matter with Y_p=0.5 (left), and for asymmetric matter with $Y_p = 0.1$ (right).

Protons repel each other. Thereby the proton density profile substantially deviates from the step-function. The proton number is enhanced near the surface of the lump.

The equation of state (EOS) for the sequence of geometric structures is shown in Fig. 3 (upper panels) as a function of the averaged baryon-number density. Note that the energy $E/A - m_N$ also includes the kinetic energy of electrons, which makes the total pressure positive. The lowest-energy configurations are selected among various geometrical structures. The most favorable configuration changes from the droplet to rod, slab, tube, bubble, and to the uniform one (the dotted thin curve) with an increase of density. The appearance of non-uniform structures in matter results in a softening of EOS: the energy per baryon gets lower up to about 15 MeV/A compared to uniform matter.

The lower panels in Fig. 3 are the cell radii R_W and the lump radii R versus averaged baryon number density. Dashed curves show the Debye screening lengths of electrons and protons calculated as $\lambda_\mathrm{D}^{e(p)} = \left(4\pi e^2 \frac{d\rho_{e(p)}^\mathrm{av}}{d\mu_{e(p)}}\right)^{-1/2}$. In all cases, except for bubbles (at $Y_p = 0.5$), R are smaller than λ_D^e. This means that the Debye screening effect of electrons inside these structures should not be pronounced.

Let us mention briefly about the neutron star matter in beta equilibrium. The apparently different feature in this case is that only the droplet configuration appears as a non-uniform structure. It should be noticed, however, that the presence or absence of the concrete pasta structure sensitively depends on the choice of the effective interaction. The droplet structure is quite similar to the case of the fixed proton mixing ratio $Y_p = 0.1$ considered above. The screening effect is very small due to the small proton ratio.[4,5]

3. Kaon Condensation at High Densities

Next let us explore high-density nuclear matter in beta equilibrium, which is expected in the inner core of neutron stars.

Kaons are Nambu-Goldstone bosons accompanying the spontaneous breaking of chiral $SU(3) \times SU(3)$ symmetry and the lightest mesons with strangeness. Their effective energy is much reduced by the kaon-nucleon interaction in nuclear medium, which is dictated by chiral symmetry. For low-energy kaons the s-wave interaction is dominant and attractive in the $I = 1$ channel, so that negatively charged kaons appear in the neutron-rich matter once the process $n \to p + K^-$ becomes energetically allowed. Since kaons are bosons, they cause the Bose-Einstein condensation at zero momentum.[8] The single-particle energy of kaons is given in a model-independent way: $\epsilon_\pm(\mathbf{p}) = \sqrt{|\mathbf{p}|^2 + m_K^{*2} + ((\rho_n + 2\rho_p)/4f^2)^2} \pm (\rho_n + 2\rho_p)/4f^2$, where m_K^* is the effective mass of kaons, $m_K^{*2} = m_K^2 - \Sigma_{KN}(\rho_n^s + \rho_p^s)/f^2$, with the KN sigma term, Σ_{KN}, and the meson decay constant, $f \equiv f_K \sim f_\pi$. The threshold condition then reads[9] $\mu_K = \epsilon_-(\mathbf{p} = 0) = \mu_n - \mu_p = \mu_e$, which means the kaon distribution function diverges at $\mathbf{p} = 0$.

3.1. *RMF treatment of nuclear matter with kaon condensation*

We explore high-density nuclear matter with kaon condensation by means of RMF model as in low-density matter. Using the same model we can discuss the non-uniform structure of nuclear matter both at low- and high-density regime in an unified way. To incorporate kaons into our RMF calculation, the thermodynamic potential of Eq. (1) is modified as

$$\Omega = \Omega_N + \Omega_M + \Omega_e + \Omega_K, \tag{16}$$

$$\Omega_K = \int d^3r \left\{ \frac{f_K^2 (\nabla\theta)^2}{2} - \frac{f_K^2 \theta^2}{2} \left[-{m_K^*}^2 + (\mu_K - V + g_{\omega K}\omega_0 g_{\rho K} R_0)^2 \right] \right\}, \tag{17}$$

where $m_K^* = m_K - g_{\sigma K}\sigma$, $\mu_K = \mu_e$, and the kaon field $K = f_K\theta/\sqrt{2}$ (f_K is the kaon decay constant). We, hereafter, neglect a rather unimportant term $\propto \sigma^2\theta^2$.The equations of motion are similar to Eqs. (7) - (13) given for the low-density case (Sec. 2). See Refs. 10, 5 for details. Additional parameters are presented in Table 1.

3.2. *Kaonic pasta structures*

Figure 4 displays typical density profiles. The neutron distribution proves to be rather flat. The proton distribution on the other hand is strongly correlated with the kaon distribution, which means that the Coulomb interaction is crucial.

In the upper panel of Fig. 5 we depict the energy per nucleon as a function of baryon number density. The dotted line indicates the case of single phase (if one assumes the absence of the mixed phase). In this case uniform matter consists of normal nuclear matter below the critical density and kaonic matter above the critical density. The cross on the dotted line ($\rho_B \simeq 0.46$ fm^{-3}) shows the critical density, i.e. the point where kaons begin to condensate in the case of single phase.

The lower panel of Fig. 5 shows the sizes of the lump R and the cell $R_{\rm W}$. The dashed lines and the dotted line in the lower panel of Fig. 5 show partial contributions to the Debye screening lengths of the electron, proton and kaon, $\lambda_{\rm D}^e$, $\lambda_{\rm D}^p$, and $\lambda_{\rm D}^K$, respectively. We see that in most cases $\lambda_{\rm D}^e$ is less than the cell size $R_{\rm W}$ but is larger than the lump size R. The proton Debye length $\lambda_{\rm D}^p$ and the kaon Debye length $\lambda_{\rm D}^K$, on the other hand, are always shorter than $R_{\rm W}$ and R.

4. Charge Screening and Surface Effects on the Pasta Structures

To demonstrate the charge screening effects we compare results of the full calculation with those given by a perturbative treatment of the Coulomb interaction often

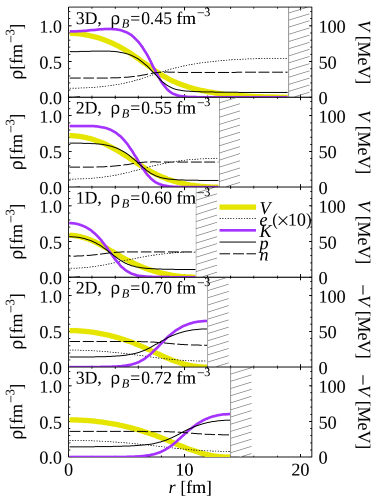

Fig. 4. Density profiles of kaonic pasta structures. Here the density does not mean charge-density but number-density of particles. The kaon optical potential U_K at the nuclear saturation density is set to be -130 MeV.

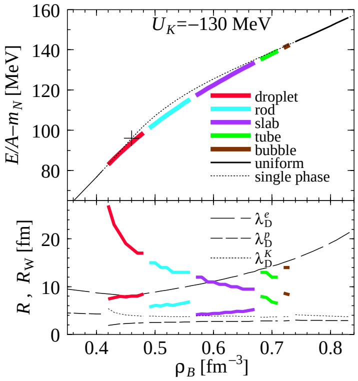

Fig. 5. Upper: binding energy per nucleon of the nuclear matter in beta equilibrium. The dotted line below the cross shows uniform normal nuclear matter and above the cross, uniform kaonic matter. Lower: lump size R (thick curves below) and cell size $R_{\rm W}$ (thick curves above). Compared are the Debye screening lengths of electron, proton and kaon. The Debye screening lengths are calculated using the explicit dependence of μ_a on ρ_a.

used in the literature, which we refer to as “no Coulomb screening” calculation. In this calculation the electric potential is discarded in equations of motion which determine the density profiles. The Coulomb energy is then added to the total energy by using the charge density profile thus determined to find the optimal value with respect to the cell size $R_{\rm W}$.

First, we discuss the case of low-density symmetric nuclear matter. In the left and the central panels of Fig. 6, compared are different treatments of the Coulomb interaction. The EOS (upper panels) as a whole shows almost no dependence on the treatments of the Coulomb interaction. However, sizes of the cell and the lump (lower panels), especially for tube and bubbles, are different. The other effect is a difference in the density range for each pasta structure. The “full” treatment of the Coulomb interaction slightly increases the density region of the nuclear pasta.

We show the same comparison for the kaonic pasta structures in Fig. 7. We

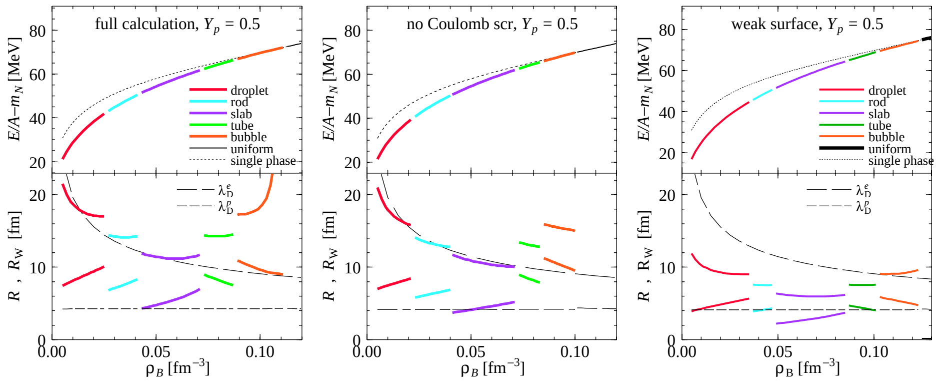

Fig. 6. Upper: binding energy per nucleon of nuclear matter. Lower: lump size R and cell size $R_{\rm W}$. The proton mixing ratio is Y_p=0.5 for all cases. From the left: “full”, “no Coulomb screening” and “weak surface” calculations. In “no Coulomb screening” calculation, the electric potential is discarded when determining the density profile and then added to evaluate the energy.

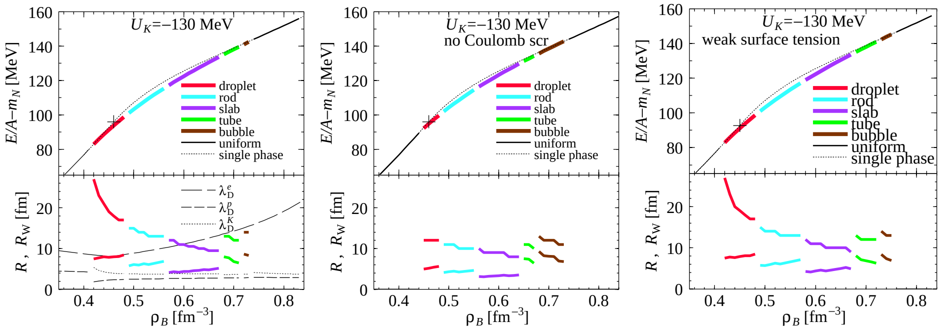

Fig. 7. The same as Fig. 6 for high-density nuclear matter in beta equilibrium.

see again that the density range of the mixed phase is narrower in the case of the "no Coulomb screening" calculation than in the full calculation, while the EOS is almost the same. A remarkable difference is the cell size, especially near the onset density of kaonic pasta, for $\rho_B < 0.5\ \mathrm{fm}^{-3}$. The cell size given by the full calculation is always larger than that given by the "no Coulomb screening" calculation.

To elucidate the screening effect, we depict the R_W dependence of the energy per nucleon in Fig. 8. In a general case of 3D droplet the Coulomb energy per particle depends on the radius by its square, while the surface energy per particle by its inverse. Therefore the sum of the Coulomb and surface energy has a U-shape (cf. "no Coulomb screening") and has a minimum at a certain radius. If the Coulomb interaction is screened, the Coulomb contribution will be suppressed (cf. the full calculation) and R_W of the minimum point gets larger. Since the cell radius is approximately proportional to the droplet radius for a given baryon density, the above argument also applies to the droplet size.

For a long time there existed a naive view that not all the Gibbs conditions can be satisfied in a description by the Maxwell construction (MC) if there are two or more independent chemical components,[11,12,13] because the local charge neutrality is implicitly assumed in it. As the result of this argument, it was suggested that a broad region of the structured mixed phase may appear in neutron stars. However, in recent papers[14,15,10,5] we have demonstrated that if one properly includes the Coulomb interaction, the MC practically satisfies the Gibbs conditions and the range of the mixed phase will be limited. The mechanism is as follows: Due to the Coulomb interaction between charged particles, their density distribution changes to reduce the Coulomb energy (Coulomb screening). Then the size of the structure gets larger and the effect of the surface becomes small. The local charge density gets smaller due to the screening. Finally the feature of the MC (local charge neutrality and no surface) is approximately achieved.

Next we consider the surface effects. If we artificially multiply meson masses m_σ, m_ω and m_ρ by a factor c_M, e.g. $c_M = 1$ (realistic case), 2.5 and 5.0, the surface tension changes. By the use of heavy meson masses, the binding energy of finite nuclei (for finite A) approaches to that of nuclear matter indicated by a thick gray line. This shows that the surface tension is reduced with increase of the meson masses, cf. Ref. 7. Using the above modified meson masses, we explore the effects of surface tension in the following. Right panels of Figs. 6 and 7 are EOS and the sizes of the cell and the lump, but now for the case of an artificially suppressed surface tension ($c_M = 5.0$). Comparing them with the left panels, we see that there is almost no difference in the EOS. However, there are two differences in the case of low-density nuclear matter. First, the density range of pasta structure is slightly broader for weaker surface tension. Secondly, the cell size with a normal surface tension is larger than the case of weaker one. It means that weaker surface tension and stronger Coulomb repulsion cause the similar effects on the cell size since the pasta structure is realized by the balance of the both.

In the case of kaonic pasta, the meson masses have very small effects. The σ,

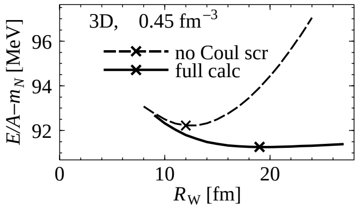

Fig. 8. The cell size R_W dependence of the energy per nucleon. Crosses on the curves indicate the minimum points.

ω and ρ mesons have less contribution to the surface tension of kaonic pasta but K-N interaction is dominant.

5. Quark Pasta Structures in the Hadron-Quark Mixed Phase

Many theoretical studies have shown that the hadronic equation of state (EOS) becomes very soft once hyperons become components of the matter. As a major consequence, the maximum mass of neutron stars (NS) predicted using the hyperonic EOS may remain below the current observational values of about 1.5 solar masses.[16] Some authors have suggested that this situation might be remedied by considering the yet unknown three-body forces (TBF) among hyperons and nucleons,[17] while other studies have shown that a quark deconfinement phase transition in hyperonic matter renders the EOS sufficiently stiff again to allow NS masses consistent with current data.[18]

We study the phase transition between hadronic and quark matter combining a Brueckner-Hartree-Fock (BHF) EOS of hyperonic hadronic matter with the standard phenomenological MIT model for the quark phase.

5.1. *Treatment of hadron-quark mixed phase*

Our theoretical framework for the hadronic matter is the nonrelativistic BHF approach based on microscopic NN, NY, and YY potentials that are fitted to scattering phase shifts, where possible. Nucleonic TBF are included in order to (slightly) shift the saturation point of purely nucleonic matter to the empirical value. With the absence of adjustable parameters, the BHF model is a reliable and well-controlled theoretical approach for the study of dense baryonic matter.

The basic input quantities in the Bethe-Goldstone equation are the NN, NY, and YY potentials. In this work we use the Argonne V_{18} NN potential supplemented by the Urbana UIX nucleonic TBF and the Nijmegen soft-core NSC89 NY potentials[19] that are well adapted to the existing experimental NY scattering data and Λ hypernuclear levels.[20,21] With these potentials, the various G-matrices are evaluated by solving numerically the Bethe-Goldstone equation. Then the total nonrelativistic hadronic energy density, ϵ_H, can be evaluated:

$$\epsilon_H = \sum_{i=n,p,\Lambda,\Sigma^-} \sum_{k<k_F^{(i)}} \left[T_i(k) + \frac{1}{2} U_i(k) \right] , \tag{18}$$

with $T_i(k) = m_i + k^2/2m_i$ and the various single-particle potentials $U_i(k)$ are determined self-consistently from the G-matrices.

For the quark EOS, we use the MIT bag model with massless u and d quarks and massive s quark with $m_s = 150$ MeV. The quark matter energy density ϵ_Q can be expressed as a sum of the kinetic term and the leading-order one-gluon-exchange term[22,23] for the interaction energy proportional to the QCD fine structure constant α_s, and the bag constant B which is the energy density difference between the perturbative vacuum and the true vacuum,

$$\epsilon_Q(\mathbf{r}) = B + \sum_f \epsilon_f(\rho_f(\mathbf{r}))\ . \tag{19}$$

The numerical procedure to determine the EOS and the geometrical structure of the MP is similar to that explained in Secs. 2 and 3. We employ a Wigner-Seitz approximation in which the whole space is divided into equivalent Wigner-Seitz cells with a given geometrical symmetry. A lump portion made of one phase is embedded in the other phase and thus the quark and hadron phases are separated in each cell. A sharp boundary is assumed between the two phases and the surface energy is taken into account in terms of a surface-tension parameter $\sigma = 40$ MeV/fm^2. We use the Thomas-Fermi approximation for the density profiles of hadrons and quarks, while the Poisson equation for the Coulomb potential V_C is explicitly solved. The energy density of the mixed phase is thus written as

$$\epsilon_M = \frac{1}{V_W}\left[\int_{V_H} d^3r\epsilon_H(\mathbf{r}) + \int_{V_Q} d^3r\epsilon_Q(\mathbf{r}) + \int_{V_W} d^3r\left(\epsilon_e(\mathbf{r}) + \frac{(\nabla V_\mathrm{C}(\mathbf{r}))^2}{8\pi e^2}\right) + \sigma S\right]\ , \tag{20}$$

where the volume of the Wigner-Seitz cell V_W is the sum of those of hadron and quark phases V_H and V_Q, and S the quark-hadron interface area. ϵ_e indicates the kinetic energy density of electron. The energy densities ϵ_H, ϵ_Q and ϵ_e are $\mathbf{r}$-dependent since they are functions of local densities $\rho_a(\mathbf{r})$ $(a = n, p, \Lambda, \Sigma^-, u, d, s, e)$. For a given density ρ_B, the optimum dimensionality of the cell, the cell size R_W, the lump size R, and the density profile of each component are searched for to give the minimum energy density. For details, see Ref. 24.

5.2. *Hadron-quark pasta structure*

Figure 9 illustrates the outcome of this procedure, showing the density profile in a 3D cell for $\rho_B = 0.4$ fm^{-3}. One can see the non-uniform density distribution of each particle species together with the finite Coulomb potential. The quark phase is negatively charged, so that d and s quarks are repelled to the phase boundary, while u quarks gather at the center. The protons in the hadron phase are attracted by the negatively charged quark phase, while the electrons are repelled.

Figure 10 compares the resulting energy per baryon of the hadron-quark MP with that of the pure hadron and quark phases over the relevant range of baryon density. The thick black curve indicates the case of the Maxwell construction, while

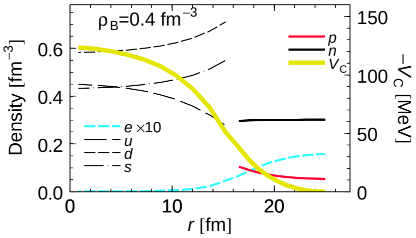

Fig. 9. Density profiles and Coulomb potential V_C within a 3D (quark droplet) Wigner-Seitz cell of the MP at $\rho_B = 0.4$ fm^{-3}. The cell radius and the droplet radius are $R_W = 26.7$ fm and $R = 17.3$ fm, respectively.

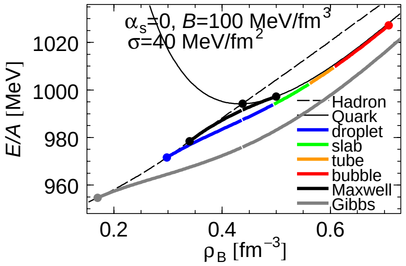

Fig. 10. EOS of the MP (thick curves) compared with pure hadron and quark phases (thin curves). Different segments of the MP are chosen by minimizing the energy.

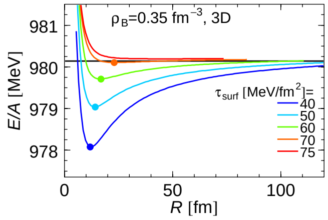

Fig. 11. Droplet radius (R) dependence of the energy per baryon for fixed baryon density $\rho_B = 0.35$ fm^{-3} and different surface tensions. The quark volume fraction $(R/R_W)^3$ is fixed for each curve. Dots on the curves show the local energy minima. The black line shows the energy of the MC case.

the colored line indicates the MP in its various geometric realizations, starting at $\rho_B = 0.326$ fm^{-3} with a quark droplet structure and ending at $\rho_B = 0.666$ fm^{-3} with a hadron bubble structure. The energy of the MP is only slightly lower than that of the MC, and the resultant EOS is similar to the MC one.

If one uses a smaller surface tension parameter σ, the energy gets lower and the density range of the MP gets wider. The limit of $\sigma = 0$ leads to a bulk application of the Gibbs conditions without the Coulomb and surface effects.[24] On the other hand, using a larger value of σ, the geometrical structures increase in size and the EOS gets closer to that of the MC case. Above a limiting value of $\sigma \approx 65$ MeV/fm^2 the structure of the MP becomes mechanically unstable[25]: for a fixed volume fraction $(R/R_W)^3$ the optimal values of R and R_W diverge and local charge neutrality is recovered in the MP, where the energy density equals that of the MC (see Fig. 11).

6. Summary

We have discussed the appearance and properties of the pasta structures and the EOS of matter in the context of the first-order phase transition in the cases of (I) low density nucleon matter, (II) kaon condensation and (III) hadron-quark deconfinement transition. We have shown a general feature that the Coulomb screening and the stronger surface tension enlarge the structure size, and limit the density region of the mixed phase. If the surface tension is strong enough, the Maxwell construction (MC) becomes effective. Actually, we have seen that the EOS of the mixed phase is close to that of the MC.

For each case, we have shown the following: The Coulomb screening effects in (II) and (III) are stronger than in (I) due to the higher charge density. The surface tension is dominated by K-N interaction for (II). Though we have not reported here, the bulk property of a compact star is strongly affected by (III).[26]

Acknowledgments

This work has been done by the collaboration with T. Tanigawa, D. N. Voskresensky T. Endo and H.-J. Schulze.

References

1. D. G. Ravenhall, C. J. Pethick and J. R. Wilson, *Phys. Rev. Lett.* **50** (1983) 2066.
2. E. K. U. Gross and R. M. Dreizler, *Density functional theory*, Plenum Press (1995).
3. R. G. Parr and W. Yang, *Density-Functional Theory of atoms and molecules*, Oxford Univ. Press, 1989.
4. T. Maruyama, T. Tatsumi, D. N. Voskresensky, T. Tanigawa and S. Chiba, *Phys. Rev.* **C72** (2005) 015802.
5. T. Maruyama, T. Tatsumi, T. Endo, and S. Chiba, *Recent Res. Devel. in Phys.* **7** (2006) 1.
6. M. Centelles and X. Viñas, *Nucl. Phys.* **A563** (1993) 173.
7. W. D. Myers and W. J. Swiatecki, *Nucl. Phys.* **A601** (1996) 141.
8. D. B. Kaplan and A. E. Nelson, *Phys. Lett.* **B175** (1986) 57; **B179** (1986) 409(E).
9. T. Muto and T. Tatsumi, *Phys. Lett.* **B283** (1992) 165.
10. T. Maruyama, T. Tatsumi, D.N. Voskresensky, T. Tanigawa, T. Endo and S. Chiba, *Phys. Rev.* **C73** (2006) 035802.
11. N. K. Glendenning and J. Schaffner-Bielich, *Phys. Rev.* **C60** (1999) 025803.
12. M. Christiansen, N. K. Glendenning and J. Schaffner-Bielich, *Phys. Rev.* **C62** (2000) 025804.
13. N. K. Glendenning, *Phys. Rev.* **D46** (1992) 1274; *Phys. Rep.* **342** (2001) 393.
14. D. N. Voskresensky, M. Yasuhira and T. Tatsumi, *Phys. Lett.* **B541** (2002) 93;
15. T. Endo, T. Maruyama, S. Chiba and T. Tatsumi, *Prog. Theor. Phys.* **115** (2006) 337.
16. D. Page, U. Geppert and F. Weber, *astro-ph*/0508056.
17. S. Nishizaki, Y. Yamamoto and T. Takatsuka, *Prog. Theor. Phys.* **105** (2001) 607; *Prog. Theor. Phys.* **108** (2002) 703.
18. G. F. Burgio, M. Baldo, P. K. Sahu, and H.-J. Schulze, *Phys. Rev.* **C66** (2002) 025802; C. Maieron, M. Baldo, G. F. Burgio, and H.-J. Schulze, *Phys. Rev.* **D70** (2004) 043010.
19. P. M. M. Maessen, Th. A. Rijken, and J. J. de Swart, *Phys. Rev.* **C40** (1989) 2226.
20. Th. A. Rijken, V. G. J. Stoks, and Y. Yamamoto, *Phys. Rev.* **C59** (1999) 21.
21. J. Cugnon, A. Lejeune, and H.-J. Schulze, *Phys. Rev.* **C62** (2000) 064308; I. Vidaña, A. Polls, A. Ramos, and H.-J. Schulze, *Phys. Rev.* **64** (2001) 044301.
22. E. Farhi and R. L. Jaffe, *Phys. Rev.* **D30** (1984) 2379; M. S. Berger and R. L. Jaffe, *Phys. Rev.* **C35** (1987) 213.
23. R. Tamagaki and T. Tatsumi, *Prog. Theor. Phys. Suppl.* **112** (1993) 277.
24. T. Maruyama, S. Chiba, H.-J. Schulze, and T. Tatsumi, *Phys. Lett.* **B**, in press; nucl-th/0702088.
25. T. Tatsumi, M. Yasuhira and D. N. Voskresensky, *Nucl. Phys.* **A718** (2003) 359c.
26. T. Maruyama, S. Chiba, H.-J. Schulze, and T. Tatsumi, arXiv/0708.3277; submitted to *Phys. Rev.* **D**.